the BEDT-TTF derivative. Furthermore, the properties indicate that the larger interlayer separation imposed by the insertion of BEDT-TTF into the bimetallic oxalato layers (16.61 Å compared to 9–10 Å in the other layered magnets) has no effect on the magnetic properties. This establishes that the magnetic ordering in these two-dimensional phases occurs within the bimetallic layers, and is triggered by the small magnetic anisotropy of the metallic ions[15].

The transport properties of the material are depicted in Fig. 3. We performed the resistance measurements on the plate-like single crystals using the standard four-contact d.c. method. The current was flowing in the plane of the layers. The conductivity at room temperature reaches a value as high as $\sim$250 S cm^{-1}. The temperature dependence of the resistance exhibits a metallic behaviour over the entire temperature range that we investigated (down to 2 K). Depending on the sample quality, the resistivity decreases by factors of about 15–25 as the temperature is decreased from 300 to 2 K. Application of a magnetic field (up to 5 T) perpendicular to the layers leads to the appearance of a negative magnetoresistance at temperatures below about 10 K (Fig. 3 inset), whereas the resistance is practically field-independent when the field is applied parallel to the layers. This feature may be caused by the presence of the internal fields generated at low temperatures by the ferromagnetic inorganic layers. We note that this is the only evident interplay between the two kinds of sublattices (ferromagnetic and conducting). No influence of the conducting sublattice on the magnetic properties has been encountered. Thus, we can say that from the electronic point of view the two sublattices are quasi-independent. This feature, characteristic of this class of molecular materials, is in sharp contrast with what is found in the classical ferromagnetic metals like iron or gadolinium, where the two electronic sublattices are strongly interacting and cannot be decoupled.

Further characterization of the material is in progress, involving measurements of resistivity and magnetoresistance at lower temperatures and in high fields, and under pressure. Moreover, to establish whether the lack of superconductivity above 2 K is intrinsic to the organic sublattice or due to the presence of the ferromagnetic oxalato layer, we are exploring the preparation of isostructural salts with a paramagnetic or even diamagnetic bimetallic oxalato layer, facilitated by the versatility of this crystal lattice. Another avenue of investigation could be the possible insertion of other organic donors that are similar to BEDT-TTF (for example, the selenium and oxygen derivatives). □

1. Williams, J. M. *et al.* Organic superconductors—new benchmarks. *Science* **252**, 1501–1508 (1991).
2. Miller, J. S. & Epstein, A. J. Organic and organometallic magnetic materials—designer magnets. *Angew. Chem. Int. Edn Engl.* **33**, 385–415 (1994).
3. Zyss, J. (ed.) *Molecular Nonlinear Optics* (Academic, New York, 1994).
4. Day, P. *et al.* Structure and properties of tris[bis(ethylenedithio)-tetrathiafulvalenium]tetrachloro-copper(II) hydrate, (BEDT-TTF)$_3$CuCl$_4$.H$_2$O: first evidence for coexistence of localized and conduction electrons in a metallic charge-transfer salt. *J. Am. Chem. Soc.* **114**, 10722–10729 (1992).
5. Coronado, E. *et. al.* Magnetic molecular metals based on the organic donor BET-TTF (BET-TTF bis(ethylenethio)tetrathiafulvalene). *Adv. Mater.* **9**, 984–987 (1997).
6. Kurmoo, M. *et al.* Superconducting and semiconducting magnetic charge transfer salts: (BEDT-TTF)$_4$AFe(C$_2$O$_4$)$_3$C$_6$H$_5$CN (A = H$_2$O, K, NH$_4$). *J. Am. Chem. Soc.* **117**, 12209–12217 (1995).
7. Kobayashi, H. *et al.* New BETS conductors with magnetic anions (BETS = bis(ethylenedithio) tetraselenafulvalene). *J. Am. Chem. Soc.* **118**, 368–377 (1996).
8. Coronado, E. *et al.* Hybrid molecular magnets obtained by insertion of decamethylmetallocenium in layered bimetallic oxalate complexes. Syntheses, structure and magnetic properties of the series [Z^{III}Cp*$_2$][M^{II}M^{III}(ox)$_3$] (Z^{III} = Co, Fe; M^{III} = Cr, Fe; M^{II} = Mn, Fe, Co, Cu, Zn; Cp* = pentamethylcyclopentadienyl). *Chem. Eur. J.* **6**, 552–563 (2000).
9. Coronado, E. *et al.* Hybrid molecular materials formed by two molecular networks. Towards multiproperty materials. *Mol. Cryst. Liq. Cryst.* **334**, 679–691 (1999).
10. Decurtins, S. *et al.* in *Magnetism: A Supramolecular Function* (ed. Kahn, O.) 487–508 (NATO ASI Ser. C484, Kluwer Academic, 1996).
11. Tamaki, H. *et al.* Design of metal-complex magnets. Syntheses and magnetic properties of mixed-metal assemblies {[NBu$_4$][MCr(ox)$_3$]}$_x$(NBu$_4^+$ = tetra(n-butyl)ammonium ion; ox^{2-} = oxalate ion; M = Mn^{2+}, Fe^{2+}, Co^{2+}, Ni^{2+}, Cu^{2+}, Zn^{2+}). *J. Am. Chem. Soc.* **114**, 6974–6979 (1992).
12. Mathonière, C. *et al.* Ferrimagnetic mixed-valency and mixed-metal tris(oxalate) iron (III) compounds: synthesis, structure and magnetism. *Inorg. Chem.* **35**, 1201–1206 (1996).
13. Beno, M. A. *et al.* The first ambient pressure organic superconductor containing oxygen in the donor molecule, β$_m$-(BEDO-TTF)$_3$Cu$_2$(NCS)$_3$, T$_c$ = 1.06 K. *Inorg. Chem.* **29**, 1599–1601 (1990).
14. Nuttall, C. J. & Day, P. Modeling stacking faults in the layered molecular-based magnets AM^{II}Fe(C$_2$O$_4$)$_3$ M^{II} = Mn, Fe; A = organic cation. *J. Solid State Chem.* **147**, 3–10 (1999).
15. Antorrena, G. *et al.* Thermal and magnetic study of mixed-metal oxalate-bridged 2d magnets. *J. Magn. Magn. Mater.* **196–197**, 581–583 (1999).

....

Direct imaging of the pores and cages of three-dimensional mesoporous materials

Yasuhiro Sakamoto*, **Mizue Kaneda***, **Osamu Terasaki***†#, **Dong Yuan Zhao**‡, **Ji Man Kim**§, **Galen Stucky**‖#, **Hyun June Shin**¶ **& Ryong Ryoo**¶#

* *Department of Physics and CIR, Tohoku University, Sendai 980-8578, Japan*
† *CREST, Japan Science and Technology Corporation, Tohoku University, Sendai 980-8578, Japan*
‡ *Department of Chemistry, Fudan University, Shanghai 200433, China*
§ *Department of Chemistry and Biochemistry, University of California, Santa Barbara, California 93106, USA, and Catalysis Center for Molecular Engineering, Korea Research Institute of Chemical Technology, Yusong, Taejon, 305-600, Korea*
‖ *Department of Chemistry and Biochemistry and Materials Department, University of California, Santa Barbara, California 93106, USA*
¶ *Materials Chemistry Laboratory, Department of Chemistry (School of Molecular Science-BK21), Korea Advanced Institute of Science and Technology, Taejon 305-701, Korea*
\# *These authors contributed equally to this work*

....

Mesostructured composite materials, with features ranging from 20 to 500 Å in size, are obtained by the kinetically controlled competitive assembly of organic and inorganic species into nanostructured domains. Short-range order is limited, and long-range order is determined by weak forces such as van der Waals or hydrogen-bonding. Three-dimensional mesoporous materials obtained by removing the organic phase are of particular interest for applications such as catalysis and chemical sensing or separation, for which structural features such as cavity shape, connectivity and ordered bimodal porosity are critical. But atomic-scale structural characterization by the usual diffraction techniques is challenging for these partially ordered materials because of the difficulty in obtaining large ($> 10\ \mu$m) single crystals, and because large repeat spacings cause diffraction intensities to fall off rapidly with scattering angle so that only limited small-angle data are available. Here we present a general approach for the direct determination of three-dimensional mesoporous structures by electron microscopy. The structure solutions are obtained uniquely without pre-assumed models or parametrization. We report high-resolution details of cage and pore structures of periodically ordered mesoporous materials[1,2], which reveal a highly ordered dual micro- and mesoscale pore structure.

It is not straightforward to obtain structural information from high-resolution electron microscopy (HREM) images for three-dimensional (3D) mesoporous materials, as the images are pro-

jected structural information of the materials along the direction of incidence. To date, the structures of the pores and cages defined by the inorganic domain structure have been inferred indirectly from absorption isotherm measurements or by using assumed structural models to generate diffraction patterns or images to compare with experimental data[3,4]. The imprecise results of this approach, particularly for X-ray or neutron scattering[5], along with the kinetic nature of the synthesis, have made it difficult to define these materials, as wide variations in structure and order of materials from apparently the same synthesis procedure may not be resolved.
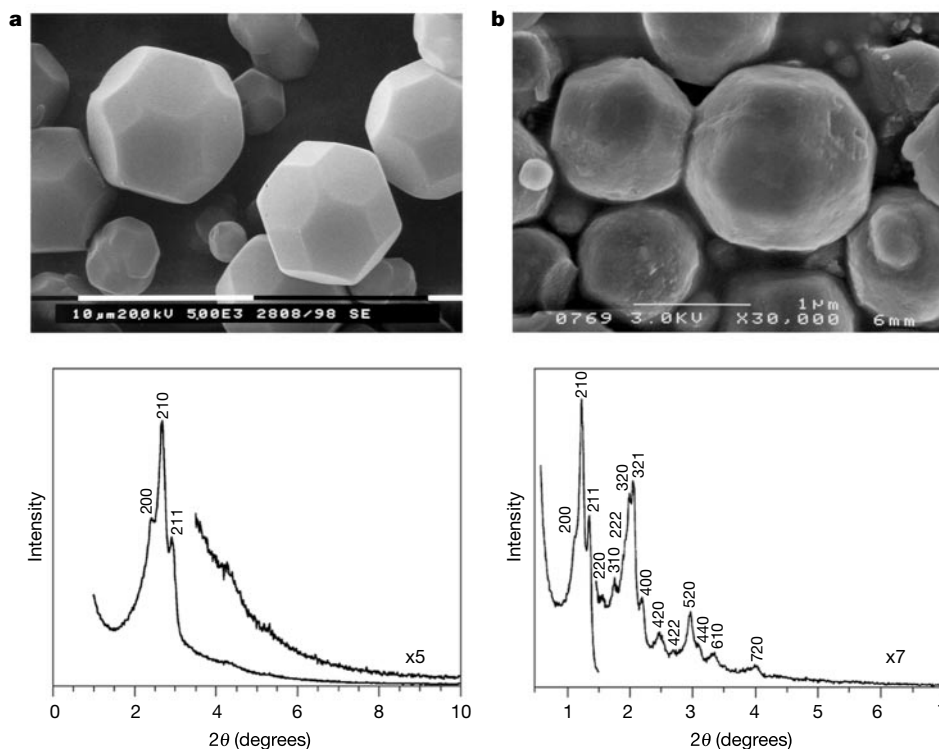

Figure 1 SEM images and X-ray powder diffraction patterns of as-synthesized SBA-1 (**a**) and SBA-6 (**b**) . The crystal morphologies are consistent with the cubic point group symmetry of $m\bar{3}m$. The X-ray diffraction patterns for these samples are indexed as $Pm\bar{3}n$ with $a = 86$ Å (as-synthesized), 73 Å (calcined) for SBA-1, and $a = 160$ Å (as-synthesized), 146 Å (calcined) for SBA-6. Unit cell constants for SBA-1 and SBA-6 decrease 15% and 9%, respectively, after calcination.
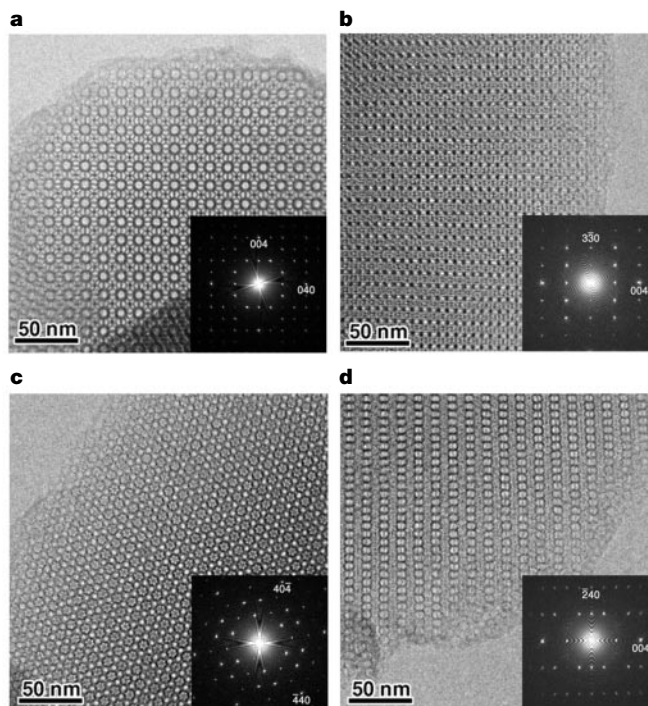

Figure 2 HREM images of SBA-6 (calcined) and their Fourier diffractograms. **a**, [100]; **b**, [110]; **c**, [111]; and **d**, [210]. The images were taken by a JEM-3010 instrument (JEOL) (spherical aberration constant $C_s = 0.6$ mm, chromatic aberration constant $C_c = 1.3$ mm, operated at 300 kV) equipped with slow-scan CCD camera.

Among the 3D mesoporous materials, SBA-1[6,7] and a mesocomposite phase that we report here (SBA-6), synthesized in acidic and basic conditions respectively, give X-ray powder diffraction patterns that can be indexed in the cubic system and which are similar to the diffraction patterns observed for cubic $Pm\bar{3}n$ globular arrays obtained in amphiphilic surfactant solution[8,9]. Another system, SBA-16 synthesized in acidic conditions with the F127 triblock copolymer, has been reported to be $Im\bar{3}m$ on the basis of X-ray and some preliminary electron-microscopy observations[1,2]. Confidence in the assignment of space groups to SBA-1 and SBA-16 was limited by the available data. Furthermore, space group symmetry is not structure and the resolved structures of 3D mesoporous cage materials have not been determined.

Mesoporous silica materials have two structural characteristics: disorder on the atomic scale (short-range) but distinct order on the mesoscopic scale (long-range). The self-organization of surfactants is an important mechanism for producing the periodic structure on the mesoscale, and this organization is highly sensitive to changes in both local and average structures on the atomic scale—it depends on synthesis conditions such as composition, temperature and pH. From a very small crystal, we can, by electron microscopy, obtain single-crystal structural information, free from the local variations that typically contribute to both a small number of reflections and large peak widths in X-ray diffraction experiments. We have developed an approach that uses electron crystallography to solve 3D structures of mesoporous materials with disordered wall structures. The 3D structural solution makes clear, at the nanoscale level, the sizes and shapes of the pores and cages, their arrangements and their connectivity, including sizes of openings.

Our method makes use of high-resolution electron microscopy (HREM), and was developed especially for periodic structural arrangements with mesoscale ordering but not necessarily short-range ordering. As diffraction intensities can give only moduli of the structure factors, while HREM images give both the amplitudes and phases of the necessary Fourier coefficients, the data collection and analysis begins with obtaining two-dimensional (2D) projections of the image of the 3D structure of the sample. Fourier-transform analysis of these 2D images collectively gives a 3D representation of the structure in reciprocal space. Once this set of structure factors with known amplitudes and phases is obtained in 3D reciprocal space, the 3D real space structure can be obtained in a straightforward way through the inverse Fourier transformation. The methodology has been successfully applied to a variety of mesoporous silica SBA structures[1,2]. Details are given here for three examples; the above-mentioned SBA-1, SBA-6 and SBA-16. Structural details for SBA-2, SBA-8, SBA-11 and several previously unreported phases will be described elsewhere.

SBA-1 and SBA-16 were synthesized following procedures based on those described previously, under acidic conditions, with a pH below the aqueous isoelectric point of silica[1,2]. An improved synthesis procedure was used for SBA-1, which differs from the one originally described[6,7] in that the synthesis was carried out at 0 °C over a period of one week[10]. The synthesis of SBA-6 has not been previously reported, and this is (to our knowledge) the first example of a cubic cage structure synthesized under basic synthesis conditions (see Methods).

The as-made (acid-synthesized) SBA-1 contains one anion for every charged surfactant with a formally neutral framework, whereas in (base-synthesized) SBA-6 the walls of the silica framework are charged to neutralize the amphiphilic gemini surfactant charge; thus the mesostructure reaction product compositions for SBA-1 and SBA-6 are distinctly different. The silica organization in the walls of the two structures differ for acid-catalysed (SBA-1) and base-catalysed (SBA-6) silica hydrolysis and polymerization[11], and the acid-polymerized silica phase has walls that are 2 to 4 times thicker because of the reduced framework charge during silica condensation.

Figure 1a and b show scanning electron microscope (SEM) images that are typical for SBA-1 and SBA-6. Both materials are crystalline at the mesoscale level, but have glass-like disorder in the walls. The HREM images are shown for SBA-6 with [100], [110], [111] and [210] incidences in Fig. 2. In order to enhance the contribution to image formation from the reflections with low-angle scattering vectors, the HREM images shown here were taken not at Scherzer focus but at underfocus (~2,000 Å). Corresponding Fourier diffractograms (moduli of Fourier transforms) are shown as insets, and they clearly show extinction conditions for the reflections. Fourier diffractograms from thin regions close to the edge of the crystal avoid the usual difficulties associated with multiple scattering contributions in electron diffraction patterns. Because of the high degree of order on the mesoscopic scale, we have confirmed independently that if the specimen is thicker than 300 Å (at operating conditions of 300 kV), multiple scattering effects become discernible even in these atomistically disordered materials, so that it is difficult to obtain the conditions for reflection solely from the electron diffraction patterns. These data for SBA-1 and SBA-6 clearly show that either $Pm\bar{3}n$ (no. 223) or $P\bar{4}3n$ (no. 218) is an allowed space group. However we conclude that the space group is $Pm\bar{3}n$, because the crystal morphologies (Fig. 1a, b) show
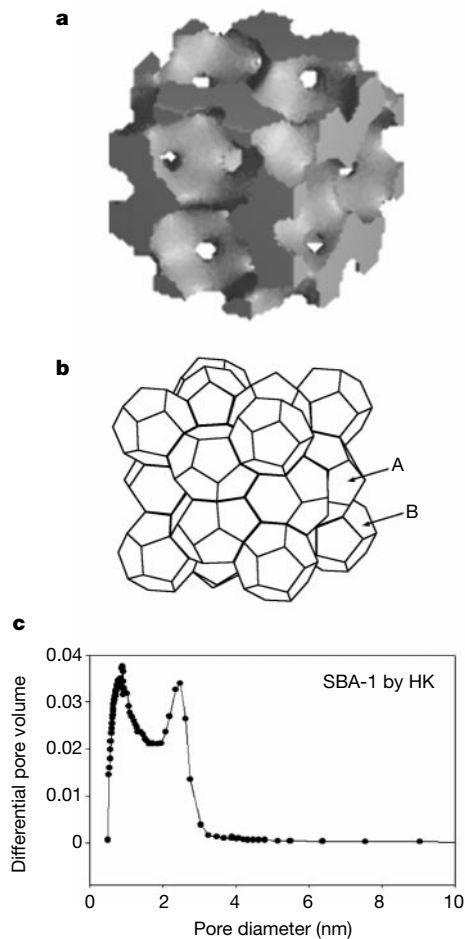

Figure 3 Direct image of 3D cages and bimodal pore structure in SBA-6 and SBA-1. **a**, 3D structure of SBA-6 obtained from the electrostatic potential map, showing large A-cages and small B-cages with associated large and small pores. **b**, Schematic drawing of the arrangement of A- and B-cages in A$_3$B type structures, where the B-cage is the smaller, with a diameter of 73 Å (SBA-6) at (0,0,0) and (1/2,1/2,1/2), and the A-cage is the larger, with a diameter of ~85 Å (SBA-6) at (1/2,0,1/4), (1/2,0,3/4), (0,1/4,1/2), (0,3/4,1/2), (1/4,1/2,0) and (3/4,1/2,0). For SBA-1, the diameters of the A and B cages are 40 Å and 33 Å, respectively. **c**, Pore sizes for the calcined SBA-1 framework determined by Horvath-Kawazoe analysis of the argon adsorption isotherm branch.

 451

point group symmetries of $m\bar{3}m$, whereas $P\bar{4}3n$ should have a point symmetry of $\bar{4}3m$.

The crystal structure factors are obtained from a set of Fourier transforms of the HREM images by correcting for the effect of an objective lens contrast transfer function (CTF). Taking the origin at the inversion centre ($m\bar{3}$), all crystal structure factors become real, that is, the phases of the structure factors are 0 or π (see Supplementary Information). At the underfocus condition used, CTF is almost linear with respect to the magnitude of the scattering vector, q, for reflections important for the Fourier sum. Therefore, for the spatial resolution that is accessible from the available diffraction data, the result is almost independent of the focus conditions. This gives 42 independent reflections out of 44 reflections with larger spacing than 20 Å. The intensities of the remaining two reflections are weak in the electron diffraction experiment.

The 3D electrostatic potential distribution for SBA-6 is obtained from the Fourier summation of the crystal structure factors (these structure factors are available as Supplementary Information). Using the pore volume of $V_p = 0.86 \text{ cm}^3 \text{ g}^{-1}$ obtained from N_2 gas adsorption data and the wall density of $D_w = 2.2 \text{ g cm}^{-3}$ determined by helium pycnometry, a threshold in the potential density is determined for differentiating between the amorphous wall and enclosed cavities, giving the 3D structure shown in Fig. 3. A-cages and B-cages, differing in size, are arranged as in an MEP clathrate type (A_3B) structure (Fig. 3b)[12].

The HREM analysis used here reveals an unusual aspect of the structures of SBA-1 and SBA-6, namely bimodal (micro-meso) porosity. In the structure of SBA-6, a B-cage is surrounded by 12 A-cages that are connected through mesoporous openings of 20 Å, while the openings between A-cages are about 33×41 Å. By the

same procedure, the 3D electrostatic potential distribution and structure of SBA-1 have been determined. In this case, $V_p = 0.60 \text{ cm}^3 \text{ g}^{-1}$, $D_w = 2.0 \text{ g cm}^{-3}$, with a greater average wall thickness based on sorption data. The mesopore size for SBA-1 determined by electron microscopy is 15×22 Å while the micropore size is 2 Å. Horvath-Kawazoe analysis of the adsorption–desorption isotherm (BET) data for SBA-1 (Fig. 3c) gives pore sizes of 24 Å and 8 Å (see Methods). There is no doubt about the bimodal porosities of these materials, although further work is needed to resolve the differences in pore diameters as determined by the BET and the HREM techniques. 3D HREM analysis gives details on asymmetric pore sizes and pore configuration that cannot be obtained by other techniques. We note that the pores of SBA-1 and SBA-6 can be made different sizes by using the appropriate surfactants.

We now apply our technique to SBA-16. Figure 4 shows HREM images for [100], [110] and [111] incidences and the corresponding Fourier diffractograms of the images from thin areas. From the observed extinction ($h + k + l = 2n + 1$), four space groups, $Im\bar{3}$, $I432$, $I\bar{4}3m$, and $Im\bar{3}m$, are possible. The morphology of the observed crystals of this material is simple cubic, indicating a point group of $m\bar{3}m$ and confirming that $Im\bar{3}m$ ($a = 133$ Å) is a suitable space group. Following the procedure described above, the 3D structure was determined and is shown in Fig. 5. Spherical cavities of 95 Å diameter are arranged in a body-centred-cubic array, and the cavities are connected through mesoporous openings of 23 Å along the [111] directions. We note that the surface with $(\cos \pi x \times \cos \pi y) + (\cos \pi x \times \cos \pi z) + (\cos \pi y \times \cos \pi z) = 0$ (Fig. 5c), which is related to the minimal surface of I-WP (body centred, wrapped package), describes well the configuration of SBA-16.

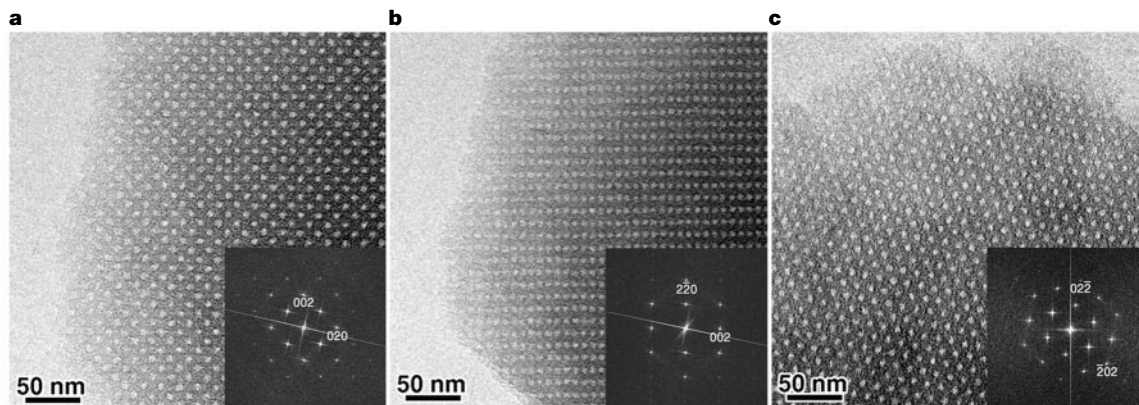The methodology described here opens a way to solve structures

Figure 4 HREM images of SBA-16 (calcined) and their Fourier diffractograms. **a**, [100]; **b**, [110]; **c**, [111]. The images were taken by a JEM-1250 instrument (JEOL) ($C_s = 1.7$ mm, $C_c = 4.0$ mm, operated at 1,250 kV) with imaging plates.
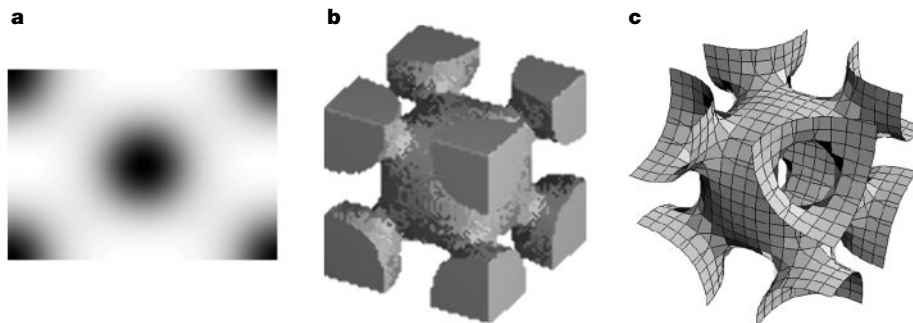

Figure 5 Direct image of 3D pore structure of SBA-16. **a**, Electrostatic potential map of SBA-16 parallel to (110) through the centre of the cell. **b**, 3D arrangement of a cavity and its interconnection. Black corresponds to the cavity. **c**, Mean cavity surface for SBA-16.

of 3D periodic mesostructured materials without assuming any structural models. The resolution for the structure is primarily limited by the quality of the HREM images, which depends on the long-range mesoscale ordering. Therefore, although further progress may give better resolution, we expect no future change to the present conclusions about the structures of SBA-1, SBA-6 and SBA-16, because the validity of the solutions does not depend on the resolution. This is a characteristic of our method that makes it different from other approaches. We also suggest that the results presented here provide a quantitative topological description of ordered mesostructured composites, and that such descriptions are essential in understanding the properties and possible applications of the composites. The resolution of periodically ordered, 3D arrangements of bimodal (meso-micro) pores in SBA-1 and SBA-6 makes it possible to consider the detailed characterization of the range of complicated porous phases that are now synthetically achievable. □

Methods

Synthesis of SBA-6

3.75 g of tetraethoxysilane (TEOS) was added with magnetic stirring to a clear solution containing 0.5 g of the gemini surfactant 18B$_{4-3-1}$ (N,N,N,N′-pentamethyl-N′-[4-(4-octadecyloxyphenoxy)-butyl]-propane-1,3-diammonium dibromide, $C_{18}H_{37}OC_6H_4OC_4H_8N(CH_3)_2C_3H_6N(CH_3)_3Br_2$), 45.4 g of doubly distilled water, and 3.69 g of benzyltrimethylammonium hydroxide at room temperature. Stirring was continued for 20 h after the addition of TEOS at room temperature. The reaction gel mixture was heated for 2 d at 80 °C without stirring. The precipitate was filtered and dried in air at room temperature.

Determination of properties

Ar adsorption and desorption isotherms were measured at 87 K. Pore volumes ($cm^3 g^{-1}$) for SBA-1, SBA-6 and SBA-16 are 0.6, 0.86 and 0.45, respectively, and the ratios of the pore volume to unit cell are respectively 0.57, 0.65 and 0.47. The surface-area/pore-volume ratio ($2.26 \times 10^9 m^{-1}$) for SBA-1 is nearly three times that of SBA-6 ($7.93 \times 10^8 m^{-1}$). The silica wall densities determined with an AccPyc 1300 helium pycnometer are also substantially different for SBA-1 ($2.00 g cm^{-3}$) and SBA-6 ($2.20 g cm^{-3}$).

1. Zhao, D. et al. Triblock copolymer syntheses of mesoporous silica with periodic 50 to 300 Ångstrom pores. Science 279, 548–552 (1998).
2. Zhao, D., Huo, Q., Feng, J., Chmelka, B. F. & Stucky, G. D. Nonionic triblock and star diblock copolymer and oligomeric surfactant syntheses of highly ordered, hydrothermally stable, mesoporous silica structures. J. Am. Chem. Soc. 120, 6024–6036 (1998).
3. Alfredsson, V. & Anderson, M. W. Structure of MCM-48 revealed by transmission electron microscopy. Chem. Mater. 8, 1141–1146 (1996).
4. Monnier, A. et al. Cooperative formation of inorganic-organic interfaces in the synthesis of silicate mesostructures. Science 261, 1299–1303 (1993).
5. Schacht, S., Janicke, M. & Schüth, F. Modeling X-ray patterns and TEM images of MCM-41. Microporous Mesoporous Mater. 22, 485–493 (1998).
6. Huo, Q. et al. Generalized syntheses of periodic surfactant/inorganic composite materials. Nature 368, 317–321 (1994).
7. Huo, Q. et al. Organization of organic molecules with inorganic molecular species into nanocomposite biphase arrays. Chem. Mater. 6, 1176–1191 (1994).
8. Auvray, X. et al. X-ray diffraction and freeze-fracture electron microscopy study of the cubic phase in the cetylpyridinium chloride formamide and cetyltrimethylammonium chloride formamide systems. Langmuir 9, 444–448 (1993).
9. Charvolin, J. & Sadoc, J. F. Periodic systems of frustrated fluid films and "micellar" cubic structures in liquid crystals. J. Phys. France 49, 521–526 (1988).
10. Ryoo, R., Kim, J. M. & Ko, C. H. in Studies in Surface Science and Catalysis Vol. 117 (eds Bonneviot, L., Béland, F., Danumah, C., Giasson, S. & Kaliaguine, S.) 151–158 (Elsevier, Amsterdam, 1998).
11. Nakanishi, K. Pore structure control of silica gels based on phase separation. J. Porous Mater. 4, 67–112 (1997).
12. Geis, H. Studies on clathrasils. III. Crystal structure of melanophlogite, a natural clathrate compound of silica. Z. Kristallogr. 164, 247–257 (1983).

Improved estimates of global ocean circulation, heat transport and mixing from hydrographic data

Alexandre Ganachaud* & **Carl Wunsch**

MIT 54-1517, 77 Massachusetts Avenue, Cambridge, Massachusetts 02139, USA

Through its ability to transport large amounts of heat, fresh water and nutrients, the ocean is an essential regulator of climate[1,2]. The pathways and mechanisms of this transport and its stability are critical issues in understanding the present state of climate and the possibilities of future changes. Recently, global high-quality hydrographic data have been gathered in the World Ocean Circulation Experiment (WOCE), to obtain an accurate picture of the present circulation. Here we combine the new data from high-resolution trans-oceanic sections and current meters with climatological wind fields, biogeochemical balances and improved a priori error estimates in an inverse model, to improve estimates of the global circulation and heat fluxes. Our solution resolves globally vertical mixing across surfaces of equal density, with coefficients in the range $(3–12) \times 10^{-4} m^2 s^{-1}$. Net deep-water production rates amount to $(15 \pm 12) \times 10^6 m^3 s^{-1}$ in the North Atlantic Ocean and $(21 \pm 6) \times 10^6 m^3 s^{-1}$ in the Southern Ocean. Our estimates provide a new reference state for future climate studies with rigorous estimates of the uncertainties.

Obtaining a consistent picture of the oceanic circulation requires adjusting thousands of parameters consistently with a priori error estimates. We present here our best estimate from selected hydrographic data (Fig. 1), which will improve with the appearance of new data. Mass flux is the most basic element of the circulation and Fig. 2 shows the best-estimate coast-to-coast integrated water mass transports for selected density classes. A volume of $15 \pm 2 Sv$ (1 sverdrup = $1 \times 10^6 m^3 s^{-1}$) of North Atlantic Deep Water (NADW) is produced in the northern North Atlantic Ocean and moves southward, entraining Antarctic Bottom Water (AABW) from below, and Antarctic Intermediate Water (AAIW) from above. As a result, the NADW is increased to $23 \pm 3 Sv$ as it exits the South Atlantic at 30° S. In the Southern Ocean, a total of $21 \pm 6 Sv$ of bottom water is formed from lower Circumpolar Deep Water (CDW)—which corresponds approximately to the lower NADW density range. Bottom water inflows (NADW + AABW mixture) to the Atlantic, Indian and Pacific oceans are $6 \pm 1.3 Sv$, $11 \pm 4 Sv$ and $7 \pm 2 Sv$, respectively. In the Indian and Pacific oceans, most of this water returns southward at deep and intermediate levels. These net values are the sums of large, strongly spatially varying, flows of opposing sign, and thus over-simplify the actual circulation; a detailed description of the circulation within each ocean basin will be published elsewhere[3,4]. Our standard model estimate of the inflow in the South Pacific Ocean is in the lower range of previously published values, but it depends directly upon the weight given to the "PO" phosphate–oxygen combination (see Methods[4,5]) conservation constraints relative to mass conservation[3]. The deep inflow to the North Pacific Ocean is also weaker than previously found[5], as a consequence of our consideration of heat and salt conservation in the northern parts of those basins.

No definition of bottom-water formation can be completely unambiguous because of the entrainment of ambient fluid during the sinking process. In our Southern Ocean definition, the bottom-

* Present address: Laboratoire de Physique des Océans, IFREMER, 29280 Plouzané, France.